

Lawrence Berkeley National Laboratory

LBL Publications

Title

Growth Dynamics and Electron Reflectivity in Ultrathin Films of Chiral Heptahelicene on Metal (100) Surfaces Studied by Spin-Polarized Low Energy Electron Microscopy

Permalink

<https://escholarship.org/uc/item/3dz3q2r1>

Journal

physica status solidi (b), 258(12)

ISSN

0370-1972

Authors

Baljozović, Miloš
Cauduro, André L Fernandes
Seibel, Johannes
[et al.](#)

Publication Date

2021-12-01

DOI

10.1002/pssb.202100263

Copyright Information

This work is made available under the terms of a Creative Commons Attribution License, available at <https://creativecommons.org/licenses/by/4.0/>

Peer reviewed

Growth Dynamics and Electron Reflectivity in Ultrathin Films of Chiral Heptahelicene on Metal (100) Surfaces Studied by Spin-Polarized Low Energy Electron Microscopy

Miloš Baljžović, André L. Fernandes Cauduro, Johannes Seibel, Anaïs Mairena, Stéphane Grass, Jérôme Lacour, Andreas K. Schmid,* and Karl-Heinz Ernst*

Interaction of electrons with chiral matter gives rise to interesting phenomena such as the chirality-induced spin selectivity. The interdependence of reflectivity of spin-polarized low energy electrons and the absolute handedness of chiral molecules is investigated. First, the growth of homochiral films of helical aromatic hydrocarbons, so-called helicenes, on a Cu(100) surface is studied by means of low energy electron microscopy and scanning tunneling microscopy in ultrahigh vacuum. As soon as the coverage exceeds one monolayer, double-layer nucleation and growth is favored such that depletion in the first layer occurs. Spatially resolved work function measurements show that second-layer patches have a lower work function than first-layer areas. Reflectivity spectra of spin-polarized electrons do not show any asymmetry between homochiral films of the enantiomers. Laterally resolved work function measurements do not confirm work function differences such as those reported earlier for photoelectron studies of chiral peptide films on ferromagnetic substrates.

1. Introduction

Molecular layers on surfaces have been widely used to study effects occurring at molecule/substrate interfaces. By controlling kinetic and thermodynamic conditions during the assembly of nano-objects, in particular molecules and atoms, various patterns of self-assembled, metal-coordinated or covalently linked structures have been obtained by careful selection of the components and surface symmetry.^[1] Not only are these patterns interesting for their topologies, they also were found to induce interesting interface phenomena. For example, (sub)monolayer films of pentacene molecules on Cu(110) were introducing significant surface state shifts dependent on the coverage.^[2] In addition, Co phthalocyanine molecules were used


to manipulate the topological interface of Bi₂Se₃ and Mn phthalocyanine molecules induced formation of Yu–Shiba–Rusinov states when adsorbed on superconducting Pb(111) substrate.^[3,4] Assembled in checkerboard manner Mn and Fe phthalocyanine molecules formed a 2D ferrimagnet via Ruderman–Kittel–Kasuya–Yosida interactions through the surface state of Au(111).^[5] Molecules were also shown to induce magnetism at Au interface “creatio ex nihilo”.^[6] Recently, it was demonstrated that molecular layers of Buckminsterfullerenes can induce ferromagnetism in Cu and Mn by beating the Stoner criteria.^[7] Molecular layers of chiral molecules, on the contrary, showed the so-called chirality-induced spin selectivity (CISS), an effect of chirality-dependent transmission of electrons through the molecules.^[8] Chiral molecules where shown to switch magnetization of underlying ferromagnetic Ni substrate.^[9] And there are even examples of enantioseparation due to differences in interaction with underlying magnetic substrates.^[10,11] Depending on the magnetization direction, differences of ≈ 80 meV in work function of chiral peptide layer on top of an out-of-plane ferromagnetic substrate were reported.^[12]

Helical aromatic hydrocarbons, so-called helicenes, have played an important role in understanding chiral crystallization when studied at surfaces by scanning tunneling microscopy (STM).^[13] At coverages above a monolayer of *rac*-[7]H, enantio-specific separation from zigzag rows with alternating enantiomers into the separate layers occurred leading to a layered racemate

M. Baljžović, J. Seibel, A. Mairena, K.-H. Ernst
Molecular Surface Science Group
Empa
Swiss Federal Laboratories for Materials Science and Technology
Dübendorf 8600, Switzerland
E-mail: karl-heinz.ernst@empa.ch

A. L. Fernandes Cauduro, A. K. Schmid
National Center for Electron Microscopy
Molecular Foundry
Lawrence Berkeley National Laboratory
Berkeley, CA 94720, USA
E-mail: akschmid@lbl.gov

S. Grass, J. Lacour
Department of Organic Chemistry
University of Geneva
Geneva 4 1211, Switzerland

 The ORCID identification number(s) for the author(s) of this article can be found under <https://doi.org/10.1002/pssb.202100263>.

© 2021 The Authors. physica status solidi (b) basic solid state physics published by Wiley-VCH GmbH. This is an open access article under the terms of the Creative Commons Attribution License, which permits use, distribution and reproduction in any medium, provided the original work is properly cited.

DOI: 10.1002/pssb.202100263

with enantiopure layers.^[14,15] Multilayers of enantiopure (*M*)- or (*P*)-[7]H on Cu(111) showed enantiomorphous moiré patterns as well as extended 3D islands on top of a completely filled second layer (Stranski–Krastanov growth mode).^[16] Apart from the interesting phenomena accompanying self-assembly and crystallization of helicenes, they also showed significant electron spin polarizations via CISS effect, piezoelectric response of single molecules or selective chiroptical responses.^[17–20]

Low energy electron microscopy (LEEM) is a powerful surface imaging technique with good spatial resolution. Originating from changes in intensity of reflected electrons as a function of their landing energy (E_0 [eV], here referred to as start voltage U_s [V]) spectral information is also available. Moreover, low electron energies make the technique very sensitive to local electronic structure.^[21,22] LEEM has been used to follow the growth of carbon-based and metallic layered materials as well as investigation of electron quantum interference effects that arose between those layers by measuring the energy dependence of electron reflectivity.^[23–33] When a spin-polarized electron beam is used for illumination (SPLEEM), the technique becomes sensitive to surface magnetization, thus allowing for complete vector-magnetometric imaging.^[34,35]

In this contribution we have investigated growth of racemic and enantiopure [7]H on Cu(100) and (12 ML)Ni/Cu(100) substrates, thereby evaluating interface effects such as changes in work function, electron reflectivity, or spin asymmetries. Exceeding 1 ML coverage, nucleation of the second layer induces initially depletion in the first layer, which was also corroborated by scanning tunneling microscopy (STM). Spatially resolved differences in work function and electron reflectivity are observed between first and second layer of [7]H on Cu(100). Moreover, neither differences in spin asymmetry nor in work function of (*P*)-[7]H on Cu(100) and on top of opposite magnetized domains on Ni(100) film are observed. As possible explanations of the absence of effects, cancellation due to opposite spin-versus-momentum alignment in reflection and signal to noise limits of work function measurements are discussed.

2. Results and Discussions

2.1. Growth of Ultrathin Heptahelicene Films on Cu(100)

The deposition of molecules has been monitored in situ by electron reflectivity changes averaged on the complete LEEM field-of-view over time. **Figure 1b** shows an example for (*P*)-[7]H growing on Cu(100) at room temperature. At the start of (*P*)-[7]H deposition (1. LEEM image), the LEEM image appears bright due to the presence of extended Cu(100) crystalline terraces with monoatomic steps observed as dark lines. Continued molecule deposition leads to monotonic reflectivity decrease until about 745 s (2. LEEM image). At the low energy used here, electron wavelength is comparable with the thickness of a monolayer, thus leading to quantum-size effects. At low coverage, mobile molecules can be regarded as virtual increase in step density, explaining the drop in reflectivity at submonolayer coverages. Nucleation and growth of extended molecular islands in the first molecular layer subsequently reduce such virtual step density, leading to an increase in reflectivity. A short saturation after about 835 s of deposition time (3. LEEM image) corresponds to completion of the first

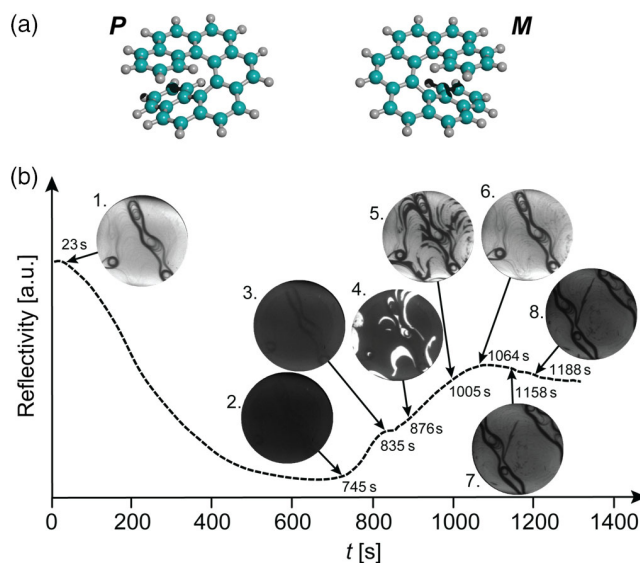


Figure 1. Time lapse of (*P*)-[7]H growth on Cu(100) monitored by LEEM. a) Ball-and-stick molecular structures of the two [7]H enantiomers. (*M*)-[7]H is the left-handed helical sense and (*P*)-[7]H is the right-handed sense. *rac*-[7]H represents a 50%:50% mixture of (*M*)-[7]H and (*P*)-[7]H. b) Average reflected electron intensity versus time of deposition together with corresponding LEEM images at different stages during the growth. $U_s = 3.2$ V, field of view is $12 \mu\text{m}$. (A small shift of the probed area occurred between frame 6. and 7.).

monolayer. The saturation reflectivity is different from the initial reflectivity due to a significant difference in electronic structure of the molecular layer with respect to the clean Cu(100) surface. With nucleation and growth of the second layer (bright tiles in 4. LEEM image after 876 s), the average reflectivity increases nearly linearly (5. LEEM image). Another intensity maximum marks the second-layer saturation after about 1064 s (6. LEEM image) before the intensity starts to drop slightly as the third layer nucleates and grows in the form of needle-shaped structures (darker features in 7. and 8. LEEM image). That the second layer is formed much faster than the first layer under constant deposition rate confirms earlier observations made for [7]H double-layer formation on the (111) surfaces of Au, Ag, and Cu.^[14,15] As soon as second-layer nucleation occurs, molecules from the first layer are transferred into the second layer, which leads to a depleted first layer at that stage. This phenomenon is captured by LEEM when the helicene growth is observed at $U_s = 4.7$ V, and it will now be discussed in more details along with **Figure 2**.

The (*P*)-[7]H deposition on Cu(100) at room temperature and $U_s = 4.7$ V reveals an intriguing effect observed in LEEM, as summarized in a sequence of images shown in **Figure 2a–d**. After 789 s from the start of deposition, formation of the first layer is observed (**Figure 2a**). The first layer appears gray at this electron energy, and it is accompanied by bright areas. After 798 s, a LEEM image (**Figure 2b**) shows the first layer almost complete, i.e., the gray area is expanded almost to the complete field-of-view at the expense of bright areas. At room temperature it is unlikely that the bright areas are representing bare substrate. These are rather disordered areas covered with mobile molecules (2D gas) in equilibrium with ordered areas. Once the coverage approaches certain

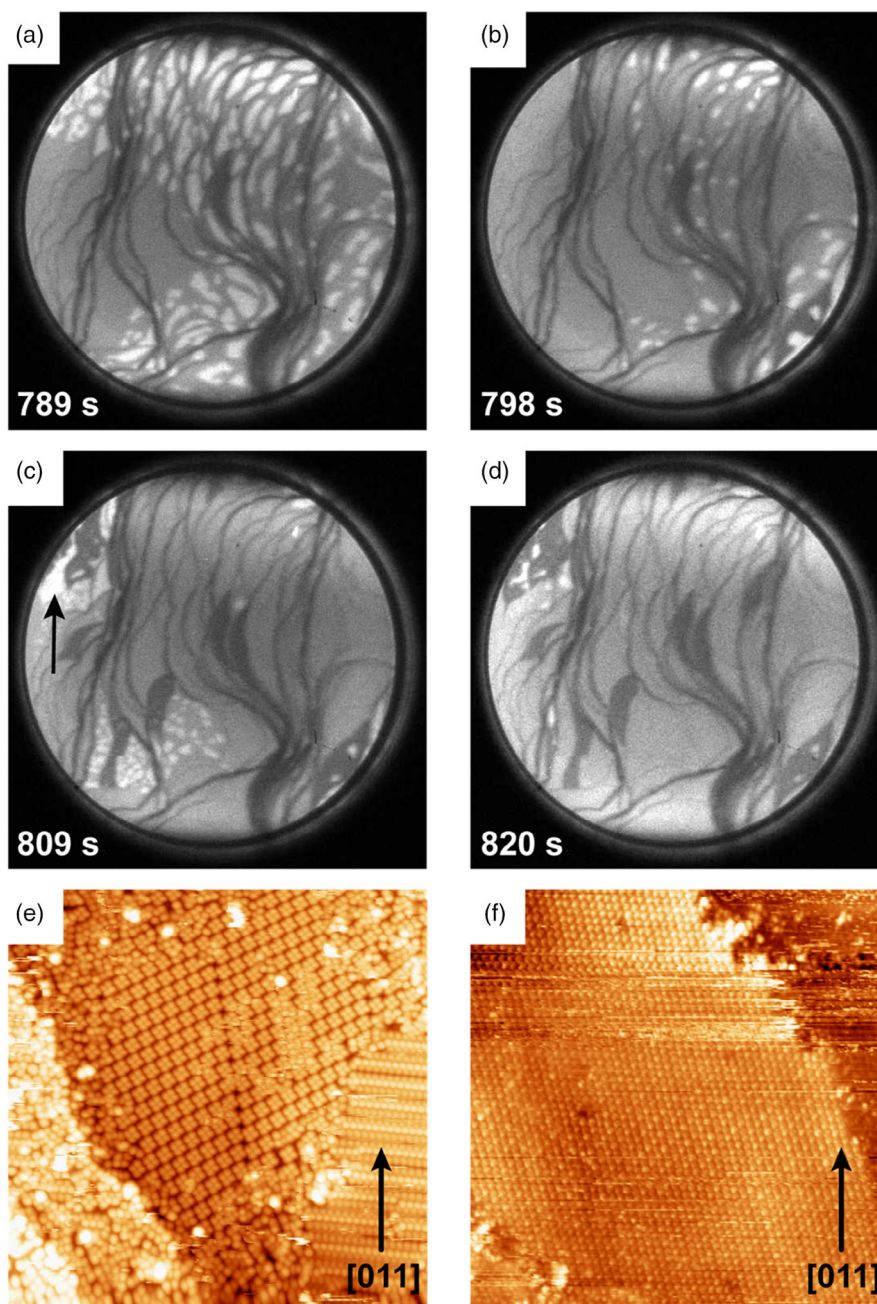


Figure 2. Sequence of consecutive LEEM ($U_s = 4.7$ V) and STM images of initial second-layer growth of [7]H on Cu(100). a–d) LEEM images acquired at different times during the growth of (P)-[7]H (contrast enhanced). The arrow in (c) points to a depleted area in the first layer induced by second-layer nucleation, which becomes filled upon further deposition (d). Values at each frame represent time elapsed from the start of molecule deposition. Image field-of-view is $12 \mu\text{m}$. e) STM image ($60 \text{ nm} \times 60 \text{ nm}$, $U = -2.9$ V, $I = 26$ pA) of (M)-[7]H at the coverage where formation of the second layer starts. f) STM image ($60 \text{ nm} \times 60 \text{ nm}$, $U = -2.9$ V, $I = 25$ pA) of (M)-[7]H of a dense second-layer island and depleted first layer next to it (upper right corner).

threshold, molecular mobility is reduced and the self-assembly into 2D islands occurs. A previous STM investigation of [7]H on Cu(100) supports this assignment.^[36] With continuing molecule deposition, second-layer molecular islands start to form once the molecular coverage exceeds the amount that can be accommodated into the first layer (Figure 2c). The second layer appears black at this electron energy. Surprisingly, the first layer shows

now disordered areas again, observed as bright areas next to the second-layer islands (Figure 2c). These bright patches represent depleted first-layer areas. That is, second-layer island size does not strictly depend on the amount of coverage beyond the filled first layer. Upon second-layer nucleation, material must be transferred from the first layer toward the double-layer islands. In earlier STM work on double layer of [7]H, first-layer depletion due to

second-layer formation was also observed on the (111) surfaces of Au, Ag, and Cu,^[14,15] as well as for pentahelicene on Cu(111).^[37] Already excess of 1% above the complete first-layer coverage induced relatively large double-layer island growth.^[37]

It is likely that the first layer underneath the second layer has a different structure and density than the first layer alone. This has been clearly shown for [7]H on Cu(111) by LEED and STM.^[15] There, both layers of the completed double layer have the same periodicity and 1.6 times the number of molecules per area than the complete first-layer before second-layer nucleation. For Cu(100) here, the second-layer nucleation STM image show an intermediate structure with molecules partly in the first and in the second layer (Figure 2). Consequently, the time to complete the second layer (counted from first-layer completion) is significantly shorter than the time needed to complete the first layer.

What is new here with respect to the previous STM studies is the fact that the first-layer depletion effect is observed for a dynamic system. In the previous STM studies, the effect was ascribed to double-layer nucleation and growth upon cooling at slightly higher temperatures than nucleation of ordered structures in the first layer. The in-situ LEEM observation here, however, is performed at room temperature. Therefore, first-layer depletion and preference of double-layer formation occur already in this highly dynamic film with enhanced molecular mobility. Such behavior suggests rather entropic effects as origin of depletion instead of previously favored enthalpic and kinetic effects.^[37] Once the second-layer islands are formed and stop growing, previously disordered bright areas in the first layer become filled and ordered and give gray contrast in LEEM again (Figure 2d).

For the 2D aggregation of [7]H on Cu(100), homochiral quadruplets have been observed for pure enantiomers as well as for the racemate.^[36] For corresponding STM studies of the double-layer growth, (*M*)-[7]H was deposited on clean Cu(100) substrates at room temperature and images with coverage above 1 ML acquired after cooling samples to 50 K. Figure 2e shows an STM image of (*M*)-[7]H revealing coexistence of the first-layer quadruplet structure,^[36] disordered areas in the first layer and an ordered row structure. Large-scale overview STM images at the same coverage shows mirror domains of the row structure with an angle of 83 ± 2 degrees between them (Figure S1a, Supporting Information). The row structure seems to be an intermediate with molecules partly still in the first layer and second layer rows on top. Further increase in coverage leads to filling up the space between the bright rows and to formation of a compact double layer (Figure 2f). High mobility next to the double-layer domain (upper right corner in Figure 2f) points again to a depleted first layer. A large-scale STM image (Figure S1b, Supporting Information) shows second-layer islands together with first-layer tetramers and disordered first-layer molecules. The effect of first-layer depletion is also observed in STM for racemic double-layer samples (Figure S1c–f, Supporting Information). It is noted again that STM and LEEM studies are not directly comparable as they are performed at different temperatures. Due to cooling before STM imaging, additional nucleation and growth phenomena may occur. Qualitatively, however, both methods reveal the phenomenon of molecular depletion in the first-layer upon second-layer nucleation.

2.2. Work Function of [7]H Films on Cu(100) and on Ni(100) Substrates

Even for materials with low density of states at the vacuum level, LEEM is well suited for measuring the work function,^[30] therefore allowing investigation of laterally resolved work function differences. The energy E_L at which the electrons land on the surface is given by

$$E_L = eU_S + E_C - \Phi_S \quad (1)$$

To have electrons interacting with the surface, the sum of the electrostatic energy gained via the applied potential eU_S plus the emitting energy at the cathode E_C needs to overcome the sample work function Φ_S (U_S is the potential difference applied between the electron cathode and the sample, the so-called start voltage). As long as the sum of $eU_S + E_C$ is smaller than Φ_S , E_L has negative values and electrons are simply repelled. As the landing energy approaches 0 eV with increasing $eU_S + E_C$, electrons start interacting with the sample and a steep drop of reflectivity is observed (so-called mirror mode transition). The work function can be determined by finding the start voltage (U_S^0) at which inflection of this reflectivity drop occurs. This is best achieved by fitting I - V LEEM curves using the complementary error function ($\text{erfc}(U)$) that takes into account energy spread of electrons emitted from the cathode.^[38] As E_L is exactly 0 eV at U_S^0 , the sample work function can be determined by

$$\Phi_S = eU_S^0 + E_C^0 \quad (2)$$

E_C^0 represents the maximum of the energy distribution of electrons emitted from the cathode.^[39,40] Combined with the spatial resolution provided by LEEM, a pixel-by-pixel fitting of I - V curves allows then for the extraction of 2D work function maps.^[39]

With respect to the clean Cu(100) surface, monolayers of pure [7]H enantiomers and *rac*-[7]H have roughly a 1 eV lower work function (Φ , Figure S2, Supporting Information). Such decrease is based on charge rearrangement in the substrate caused by Pauli repulsion, as observed for similar aromatic adsorbates.^[41] **Figure 3** shows a LEEM image (Figure 3a), a Φ -map (Figure 3b), and a line profile (Figure 3c), which highlight differences in Φ between the first and the second layer of (*P*)-[7]H on Cu(100). The samples have been prepared such that the depletion in the first layer was filled. In the 2D Φ difference map, the work function color scale is normalized to the average Φ of dark first-layer regions and plotted pixel-by-pixel in color (Figure 3b) according to the color scale shown below panel (b). Then a 20 pixels \times 120 pixels line profile is constructed such that it crosses both first and second-layer regions (Figure 3c). The according analysis for (*M*)-[7]H is shown in Figure S3, Supporting Information. For both enantiomers, the work function of a double layer is found to be 15 ± 5 meV lower than that of the closed-packed monolayer. In a pure dipole model, the second layer usually causes a reversal in work function change, due to depolarization effects. The further decrease here is therefore attributed to a structural change of density in the monolayer, in accordance with the STM observation of a transition from a quadruplet structure to the row structure (Figure 2e).

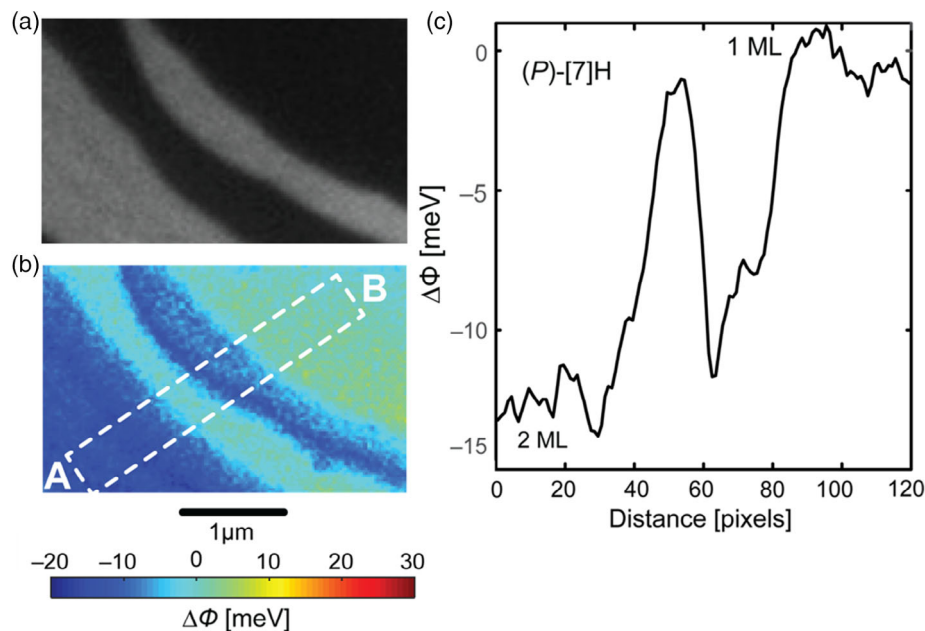


Figure 3. LEEM image, 2D work function differences map ($\Delta\Phi$ [eV] = $\Phi - \Phi_{\text{dark}}$) and line profile of a (*P*)-[7]H film. a) LEEM bright-field image of (*P*)-[7]H showing 2 ML tiles (bright) and first layer (dark). b) Pixel-by-pixel map of $\Delta\Phi$ of the film shown in (a) plotted in color scale shown below panel (e), exhibiting work function contrast between the two layers. c) 20 pixels \times 120 pixels line profile showing that the double-layer regions have 15 ± 5 meV lower work function with respect to the 1 ML regions.

2.3. Spin-Polarization-Resolved Electron Reflectivity and Work Function Differences on Magnetic Films

In photoelectron emission experiments through enantiopure [7]H layers, a profound electron spin selectivity has been observed recently.^[18] Therefore, it is interesting to see if there are asymmetries in electron reflection from homochiral layers of [7]H. Reflectivity spectra represent a fingerprint of the unoccupied density of states with momentum in the surface normal direction. Beam electrons propagating in these states are lost to the reflectivity measurements, thus high reflectivity indicates low density of states and vice versa. **Figure 4** shows reflectivity spectra as function of start voltage for 1 ML and 2 ML of the (*P*)-enantiomer and the racemate. The respective spectra for the (*M*)-enantiomer are shown in Figure S4, Supporting Information. The racemate serves as reference, as no spin selectivity can be expected for its films. However, even for the enantiopure samples the reflectivity curves are identical for spin-up and spin-down polarizations of the electron beam. Such result can be indeed expected for a perfectly reflected beam because at the molecular reference frame electron momentum-versus-spin alignment of an incoming electron is reversed upon reflection; consequently, there is no CISS effect for electron reflection. Any effect is cancelled due to the opposite alignment of electron spin polarization and momentum upon reflection. The latter possibility can be discussed on the basis of the phase accumulation model, which is widely accepted for SPLEEM reflectivity in thin film systems.^[30,42] In this picture a thin film system is described as a 1D staircase potential, accounting for the energy of the electron in vacuum and the inner potentials of the film and substrate materials. A reflectivity measurement such as SPLEEM is then described by superposition of two contributions, 1) the Bloch state transmission and reflection at the step

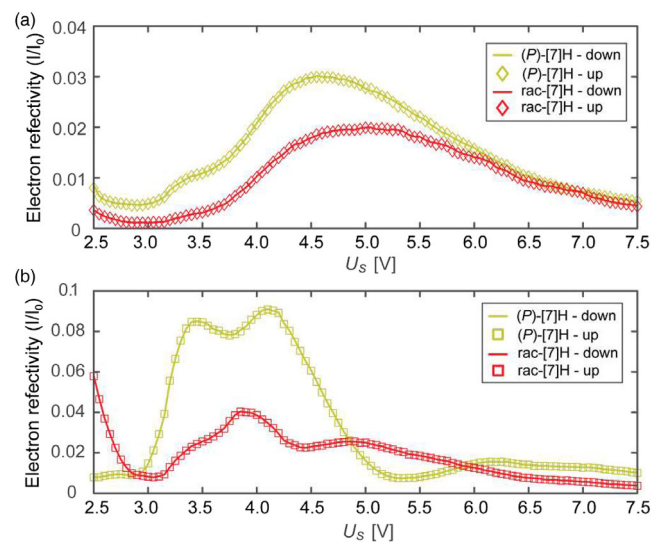


Figure 4. SPLEEM reflectivity versus start voltage spectra. a) SPLEEM reflectivity versus start voltage plots for 1 ML films of (*P*)-[7]H with spin-down (solid yellow line) and spin-up (yellow diamonds) electron polarizations and *rac*-[7]H with spin-down (solid red line) and spin-up (red diamonds) electron polarizations. b) SPLEEM reflectivity versus start voltage spectra for 2 ML films of (*P*)-[7]H with spin-down (solid green line) and spin-up (green squares) electron polarizations and *rac*-[7]H with spin-down (solid red line) and spin-up (red squares) electron polarizations. The reflectivity in the mirror mode (I_0 , 100% reflection) is used for intensity normalization. Notably, no difference is observed between datasets obtained with opposite electron polarizations.

from vacuum level to the inner potential of the thin film and 2) transmission and reflection at the step from the inner potential

of the film to that of the substrate. If one assumes spin-independent inner potentials, then the two reflectivity contributions in this model do not imply any spin dependence. CISS effects may still be expected to occur during transmission through the chiral film material.^[8] However, the only contribution that involves transmission and that is observed in a SPLEEM image is the Bloch wave that was reflected at the film/substrate interface. This contribution propagates the film twice, before and after reflection at the film/substrate interface. As upon reflection at the film/substrate interface the momentum vector is reversed (k becomes $-k$), but the spin is conserved (s remains s , $-s$ remains $-s$), their relative alignment is different upon the reflection. For the fixed molecular chirality, such change in alignment would lead to the opposite sign of the CISS effect.^[8] Therefore, a possible CISS effect in electron propagation in the chiral film would be canceled and therefore unobservable in SPLEEM reflectivity measurements.

Differences in work function on magnetic surfaces have been measured previously for chiral peptides by photoelectron emission with unpolarized light.^[12] In such experiments, Φ is determined by the difference of the photon energy and the secondary cutoff energy ($E_{\text{kin}} = 0$; $E_{\text{B}} = \text{max.}$)

$$\Phi = h\nu - E_{\text{B}}^{\text{max}} \quad (3)$$

In case of a preferred spin orientation of transmitted electrons induced by the helical sense of the chiral film (CISS effect), the combination with the spin state of majority spin electrons of a ferromagnetic substrate will cause a difference in the energy barrier for transmission of oppositely polarized electrons. Consequently, a difference in Φ is expected for opposite handed films on a ferromagnetic substrate.^[12] As LEEM experiments are known to provide comparable work function values as those obtained in photoemission experiments,^[39] a difference in Φ is expected for a single homochiral film on domains with opposite out-of-plane magnetization. Despite the absence of CISS in electron reflectivity experiments, there is a spin polarization at the interface of the ferromagnet surface and the chiral molecule. The surface potential (i.e., alignment of the vacuum level) depends on the combination of out-of-plane magnetization direction and sense of helicity.^[12]

To investigate the dependence of Φ on the magnetization direction of a Ni substrate, a SPLEEM study of the (*P*)-[7]H/Ni(100) interface was conducted. Molecules at the coverage equal to 1 ML were deposited onto a 12 ML thick Ni film grown on a Cu(100) substrate. At this molecular coverage, SPLEEM can still resolve the orientation of Ni magnetic domains (up/down) at $U_{\text{S}} = 7.5$ V (Figure 5a). Notably, the work function (more precisely, U_{S}^0) map shown in Figure 5b is uniform, i.e., no evidence of work function difference upon reversal of the magnetization direction is seen. However, a noise of about ± 15 meV (green to red, i.e., 2.55–2.58 V) is observed and differences below 30 meV remain therefore unobservable. The magnitude of this noise is probably due to roughness of the molecular layer, as [7]H on Ni surfaces has low mobility and does not form well-ordered films. In addition, the I - V curves in Figure 5c of the selected regions in opposite magnetized Ni domains (black and blue rectangles in Figure 5a) overlap on each other very well, demonstrating no apparent work function difference above 30 meV. The same

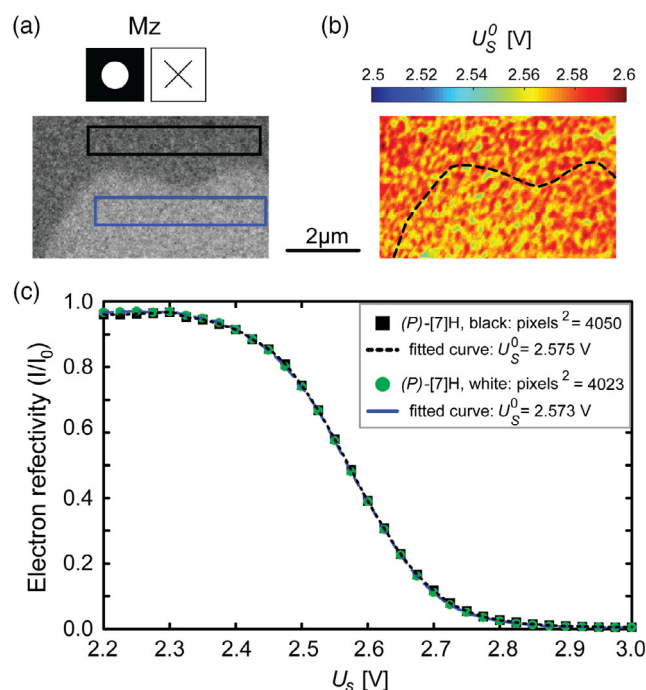


Figure 5. SPLEEM analysis of 1 ML of (*P*)-[7]H on a Ni(100)/Cu(100) substrate (12 ML Ni). a) SPLEEM image of (*P*)-[7]H/Ni(100)/Cu(100) ($U_{\text{S}} = 7.5$ V). Dark domain represents magnetization out-of-plane (pointing up), while bright domain represents magnetization out-of-plane (pointing down). Black and blue rectangles mark regions from which the I - V spectra shown in (c) were measured. b) Pixel-by-pixel 2D map of the work function of the area shown in (a). The black dashed line marks the ferromagnetic domain boundary as observed in (a). c) Normalized LEEM intensity versus start voltage acquired from regions marked by black and blue boxes in (a). I_0 is the reflectivity in the mirror mode (100% reflection) and is used for intensity normalization. The black squares and the blue circles represent the normalized average intensity of about 4000 pixels². Complementary error function fits used to measure work function from the LEEM intensity drop-off are plotted as dashed black and blue lines. The perfect overlap of these lines indicates identical values of the work function independent of Ni magnetization direction.

conclusion derives from the U_{S}^0 values obtained by the complementary error function fittings of I - V curves.

3. Conclusion

Exceeding the maximum coverage of [7]H molecules that can be accommodated into a single layer on the Cu(100) surface, the system undergoes at room temperature a critical transition toward more double-layer nucleation and growth. Increased electron reflectivity observed by SPLEEM in the first layer suggests a depletion of molecules in the first layer near second-layer islands which is confirmed by STM studies at cryogenic temperatures. Laterally resolved work function maps show that double-layer islands exhibit a 15 ± 5 meV lower work function than the first layer.

Spin-dependent reflectivity spectra acquired from homochiral films as well as from the racemic layers do not show any asymmetries, neither in spin polarization nor between enantiomers.

The absence of a CISS effect in our electron reflectivity measurements does not preclude the possible existence of spin selective transport in helicene films, as it can be attributed to cancellation resulting from reversal of electron momentum-versus-spin alignment upon reflection at the chiral film/substrate interface. Finally, no differences in work function above 30 meV for homo-chiral films of [7]H with respect to out-of-plane ferromagnetic domains in a Ni(100) film are observed.

4. Experimental Section

Heptahelicene Enantioseparation: *rac*-[7]H was purchased from Chiracon GmbH (Luckenwalde, Germany). Resolution of the (*M*)- and (*P*)-enantiomers was performed using an Agilent 1260 Infinity II high-performance liquid chromatography (HPLC) system using an UV detector at 254.4 nm under semipreparative conditions. The best separation was achieved with a semipreparative Chiralpak IG column (250 × 10 mm, 5 μm) and a 4:1 solvent mixture of dichloromethane and hexane with a 2 mL min⁻¹ flow rate. Temperature was set and controlled at 25 °C, injection at 400 μL per run. Under those conditions, well-separated fractions were obtained with retention times of 15 and 19 min for each enantiomer affording, from 130 mg of racemic material, 53 and 44 mg of the first and second eluted enantiomers, respectively. The enantiomeric purity (>99.9%) of the isolated fractions was verified using the following conditions, Chiralpak IG (250 × 4.6 mm 5 μm), 1 mL min⁻¹, a 4:1 CH₂Cl₂:hexane (Figure S5, Supporting Information).

The assignment of absolute handedness has been performed with UV/vis circular dichroism in comparison with previously performed experimental and modeled vibrational circular dichroism spectra.^[43]

Substrate Preparation: The Cu(100) surfaces have been cleaned by repetitive Ar⁺ ion sputtering and annealing at 550 °C. In the first several cycles of sputtering, small amount of oxygen was added for carbon removal. The cleanliness of the substrate was confirmed by Auger spectroscopy. (*M*)-, (*P*)-, and *rac*-[7]H molecules were deposited on substrates kept at room temperature from home-made effusion cells held at 170 °C. The coverage was adjusted by evaporation times and corroborated by LEEM, Auger spectroscopy or STM. For LEEM measurements, deposition was performed directly in the SPLEEM chamber and coverage was monitored in situ by LEEM intensity/reflectivity changes. For the Ni(100)/Cu(100) sample preparation, Ni was deposited from a home-made E-beam evaporator onto a clean Cu(100) substrate. The 12 ML Ni coverage was determined by LEEM oscillations in step density on the surface.^[44]

SPLEEM: Measurements were performed at the National Center for Electron Microscopy of the Lawrence Berkeley National Laboratory. Cesium GaAs cathode with the peak of energy distribution of emitted electrons at around $E_c^0 = 1.4$ eV was used as an electron source.^[45] All samples were prepared under ultrahigh vacuum (UHV) conditions directly in the SPLEEM chamber, with a base pressure lower than 1.0×10^{-10} mbar. Samples were initially corrected for the tilt and electron beam aligned for homogeneous irradiation over the complete field of view with out-of-plane polarized electron spins.

STM Measurements: STM experiments were performed under ultrahigh vacuum conditions (base pressure lower than 1.0×10^{-10} mbar) in constant-current mode with electrochemically etched tungsten tips and the bias voltage applied to the sample using variable-temperature STM (Omicron Nanotechnology GmbH) operated at 50 K. The samples were prepared in situ in the same chamber.

Supporting Information

Supporting Information is available from the Wiley Online Library or from the author.

Acknowledgements

In memory of Ward Plummer and David A. Shirley.

M.B. and A.L.F.C. contributed equally to this work. Work at the Molecular Foundry was supported by the Office of Science, Office of Basic Energy Sciences, of the US Department of Energy under contract no. DE-AC02-05CH11231. Part of this work was supported from the Swiss National Science Foundation (grants CRII5_173720 and 182082) and the University of Geneva.

Open access funding provided by Lib4RI Library for the Research Institutes within the ETH Domain Eawag Empa PSI and WSL.

[Correction added on April 7, 2022, after first online publication: CSAL funding statement has been added.]

Conflict of Interest

The authors declare no conflict of interest.

Data Availability Statement

Research data are not shared.

Keywords

chirality, helicenes, low energy electron microscopy, spin-polarized electrons, spin selectivity, SPLEEM, STM

Received: June 6, 2021

Revised: September 16, 2021

Published online: October 15, 2021

- [1] J. V. Barth, G. Costantini, K. Kern, *Nature* **2005**, *437*, 671.
- [2] A. Scheybal, K. Müller, R. Bertschinger, M. Wahl, A. Bendounan, P. Aebi, T. A. Jung, *Phys. Rev. B* **2009**, *79*, 115406.
- [3] M. Caputo, M. Panighel, S. Lisi, L. Khalil, G. D. Santo, E. Papalazarou, A. Hruban, M. Konczykowski, L. Krusin-Elbaum, Z. S. Aliev, M. B. Babanly, M. M. Otrokov, A. Politano, E. V. Chulkov, A. Arnau, V. Marinova, P. K. Das, J. Fujii, I. Vobornik, L. Perfetti, A. Mugarza, A. Goldoni, M. Marsi, *Nano Lett.* **2016**, *16*, 3409.
- [4] N. Hatter, B. W. Heinrich, M. Ruby, J. I. Pascual, K. J. Franke, *Nat. Commun.* **2015**, *6*, 8988.
- [5] J. Girovsky, J. Nowakowski, M. E. Ali, M. Baljovic, H. R. Rossmann, T. Nijs, E. A. Aebi, S. Nowakowska, D. Siewert, G. Srivastava, C. Wäckerlin, J. Dreiser, S. Decurtins, S.-X. Liu, P. M. Oppeneer, T. A. Jung, N. Ballav, *Nat. Commun.* **2017**, *8*, 15388.
- [6] I. Carmeli, G. Leitner, R. Naaman, S. Reich, Z. Vager, *J. Chem. Phys.* **2003**, *118*, 10372.
- [7] F. A. Ma'Mari, T. Moorsom, G. Teobaldi, W. Deacon, T. Prokscha, H. Luetkens, S. Lee, G. E. Sterbinsky, D. A. Arena, D. A. MacLaren, M. Flokstra, M. Ali, M. C. Wheeler, G. Burnell, B. J. Hickey, O. Cespedes, *Nature* **2015**, *524*, 69.
- [8] R. Naaman, D. H. Waldeck, *J. Phys. Chem. Lett.* **2012**, *3*, 2178.
- [9] O. Ben Dor, S. Yochelis, A. Radko, K. Vankayala, E. Capua, A. Capua, S.-H. Yang, L. T. Baczewski, S. S. P. Parkin, R. Naaman, Y. Paltiel, *Nat. Commun.* **2017**, *8*, 14567.
- [10] K. Banerjee-Ghosh, O. B. Dor, F. Tassinari, E. Capua, S. Yochelis, A. Capua, S.-H. Yang, S. S. P. Parkin, S. Sarkar, L. Kronik, L. T. Baczewski, R. Naaman, Y. Paltiel, *Science* **2018**, *360*, 1331.
- [11] F. Tassinari, J. Steidel, S. Paltiel, C. Fontanesi, M. Lahav, Y. Paltiel, R. Naaman, *Chem. Sci.* **2019**, *10*, 5246.

- [12] J. M. Abendroth, K. M. Cheung, D. M. Stermer, M. S. El Hadri, C. Zhao, E. E. Fullerton, P. S. Weiss, *J. Am. Chem. Soc.* **2019**, *141*, 3863.
- [13] K.-H. Ernst, *Acc. Chem. Res.* **2016**, *49*, 1182.
- [14] J. Seibel, M. Parschau, K.-H. Ernst, *Chirality* **2020**, *32*, 975.
- [15] M. Parschau, K.-H. Ernst, *Angew. Chem. Int. Ed.* **2015**, *54*, 14422.
- [16] M. Parschau, U. Ellerbeck, K.-H. Ernst, *Colloids Surf. A* **2010**, *354*, 240.
- [17] V. Kiran, S. P. Mathew, S. R. Cohen, I. H. Delgado, J. Lacour, R. Naaman, *Adv. Mater.* **2016**, *28*, 1957.
- [18] M. Kettner, V. V. Maslyuk, D. Nürenberg, J. Seibel, R. Gutierrez, G. Cuniberti, K.-H. Ernst, H. Zacharias, *J. Phys. Chem. Lett.* **2018**, *9*, 2025.
- [19] O. Stetsovych, P. Mutombo, M. Švec, M. Šámal, J. Nejedlý, I. Čísařová, H. Vázquez, M. Moro-Lagares, J. Berger, J. Vacek, I. G. Starý, I. Starý, P. Jelínek, *J. Am. Chem. Soc.* **2018**, *140*, 940.
- [20] Y. Yang, R. C. da Costa, M. J. Fuchter, A. J. Campbell, *Nat. Photonics* **2013**, *7*, 634.
- [21] E. Bauer, *Rep. Prog. Phys.* **1994**, *57*, 895.
- [22] E. Bauer, in *Science of Microscopy* (Eds: P. W. Hawkes, J. C. H. Spence), Springer, New York, NY **2007**, pp. 605–656.
- [23] A. A. Zakharov, A. Mikkelsen, J. N. Andersen, *J. Electron Spectrosc. Relat. Phenom.* **2012**, *185*, 417.
- [24] F.-J. Meyer zu Heringdorf, M. C. Reuter, R. M. Tromp, *Nature* **2001**, *412*, 517.
- [25] M. L. Ng, A. B. Preobrajenski, A. A. Zakharov, A. S. Vinogradov, S. A. Krasnikov, A. A. Cafolla, N. Mårtensson, *Phys. Rev. B* **2010**, *81*, 115449.
- [26] C. Virojanadara, M. Syväjarvi, R. Yakimova, L. I. Johansson, A. A. Zakharov, T. Balasubramanian, *Phys. Rev. B* **2008**, *78*, 245403.
- [27] G. Hlawacek, F. S. Khokhar, R. van Gastel, H. J. W. Zandvliet, B. Poelsema, C. Teichert, in *Small Organic Molecules on Surfaces: Fundamentals and Applications* (Eds: H. Sitter, C. Draxl, M. Ramsey), Springer, Berlin, Heidelberg **2013**, pp. 107–139.
- [28] J. Jobst, J. Kautz, D. Geelen, R. M. Tromp, S. J. van der Molen, *Nat. Commun.* **2015**, *6*, 1.
- [29] H. Hibino, H. Kageshima, F. Maeda, M. Nagase, Y. Kobayashi, H. Yamaguchi, *Phys. Rev. B* **2008**, *77*, 075413.
- [30] J. Xu, F. Lou, M. Jia, G. Chen, C. Zhou, Q. Li, K. Liu, A. K. Schmid, H. Xiang, Y. Wu, *AIP Adv.* **2020**, *10*, 045204.
- [31] A. Haags, L. A. Rochford, J. Felter, P. J. Blowey, D. A. Duncan, D. P. Woodruff, C. Kumpf, *New J. Phys.* **2020**, *22*, 063028.
- [32] M. S. Altman, W. F. Chung, Z. Q. He, H. C. Poon, S. Y. Tong, *Appl. Surf. Sci.* **2001**, *169–170*, 82.
- [33] W. F. Chung, Y. J. Feng, H. C. Poon, C. T. Chan, S. Y. Tong, M. S. Altman, *Phys. Rev. Lett.* **2003**, *90*, 216105.
- [34] T. Duden, E. Bauer, *Rev. Sci. Instrum.* **1995**, *66*, 2861.
- [35] N. Rougemaille, A. Schmid, *EPJ Appl. Phys.* **2010**, *50*, 20101.
- [36] J. Seibel, L. Zoppi, K.-H. Ernst, *Chem. Commun.* **2014**, *50*, 8751.
- [37] A. Mairena, L. Zoppi, J. Seibel, A. F. Tröster, K. Grenader, M. Parschau, A. Terfort, K.-H. Ernst, *ACS Nano* **2017**, *11*, 865.
- [38] A. L. F. Cauduro, R. Dos Reis, G. Chen, A. K. Schmid, H.-G. Rubahn, M. Madsen, *Ultramicroscopy* **2017**, *183*, 99.
- [39] A. L. Fernandes Cauduro, L. H. Hess, D. F. Ogletree, J. W. Schwede, A. K. Schmid, *Appl. Phys. Lett.* **2019**, *115*, 071602.
- [40] J. Jobst, L. M. Boers, C. Yin, J. Aarts, R. M. Tromp, S. J. van der Molen, *Ultramicroscopy* **2019**, *200*, 43.
- [41] a) G. Witte, S. Lukas, P. S. Bagus, C. Wöll, *Appl. Phys. Lett.* **2005**, *87*, 263502; b) P. S. Bagus, K. Hermann, C. Wöll, *J. Chem. Phys.* **2005**, *123*, 184109; c) R. Caputo, B. P. Prascher, V. Staemmler, P. S. Bagus, C. Wöll, *J. Phys. Chem. A* **2007**, *111*, 12778; d) L. Zoppi, Q. Stöckl, A. Mairena, O. Allemann, J. S. Siegel, K. K. Baldrige, K.-H. Ernst, *J. Phys. Chem. B* **2017**, *122*, 871; e) A. Mairena, L. Zoppi, S. Lampart, K. K. Baldrige, J. S. Siegel, K.-H. Ernst, *Chem. Eur. J.* **2019**, *25*, 11555; f) T. Bauert, L. Zoppi, G. Koller, A. Garcia, K. K. Baldrige, K.-H. Ernst, *J. Phys. Chem. Lett.* **2011**, *2*, 2805.
- [42] a) R. E. Thomas, *J. Appl. Phys.* **1970**, *41*, 5330; b) B. T. Jonker, N. C. Bartelt, R. L. Park, *Surf. Sci.* **1983**, *125*, 183; c) T. Scheunemann, R. Feder, J. Henk, E. Bauer, T. Duden, H. Pinkvos, H. Poppa, K. Wurm, *Solid State Commun* **1997**, *104*, 787; d) R. Zdyb, E. Bauer, *Phys. Rev. Lett.* **2002**, *88*, 166403.
- [43] a) R. H. Martin, M. J. Marchant, *Tetrahedron* **1974**, *30*, 343; b) T. Bürgi, A. Urakawa, B. Behzadi, K.-H. Ernst, A. Baiker, *New J. Chem.* **2004**, *28*, 332.
- [44] K. L. Man, M. S. Altman, H. Poppa, *Surf. Sci.* **2001**, *480*, 163.
- [45] R. C. Eden, J. L. Moll, W. E. Spicer, *Phys. Rev. Lett.* **1967**, *18*, 597.